SUPPLEMENTARY DOCUMENT

Nanocrystalline and Mesoporous (Ba,Sr)(Sn,Mn)O_3 perovskite solid solution: A potential n-type semiconductor for room temperature ethanol sensing applications

Nehal Ashok Waghchoure [a)] and Kampurath Poduvattil Jayadevan [*a]

[a)] *Energy and Environmental Chemistry Laboratory, Department of Chemistry Birla Institute of Technology and Science, NH17B, Zuarinagar, Vasco da Gama, 403726, INDIA.*

[*]*Author for correspondence:* jayadev@goa.bits-pilani.ac.in

• XRD plots of Mn-doped/undoped $Ba_{0.98}Sr_{0.02}SnO_3$ perovskite

The XRD plots of Mn-doped/undoped $Ba_{0.98}Sr_{0.02}SnO_3$ perovskites. It shows that as the concentration of Mn increases ($x > 0.05$ in $Ba_{0.98}Sr_{0.02}Sn_{1-x}Mn_xO_3$), the XRD shows the presence of SnO_2 as seen in Fig. S1a. It can be seen that as the Mn concentration increases, the carbonate peak at c.a. 24° flattens.

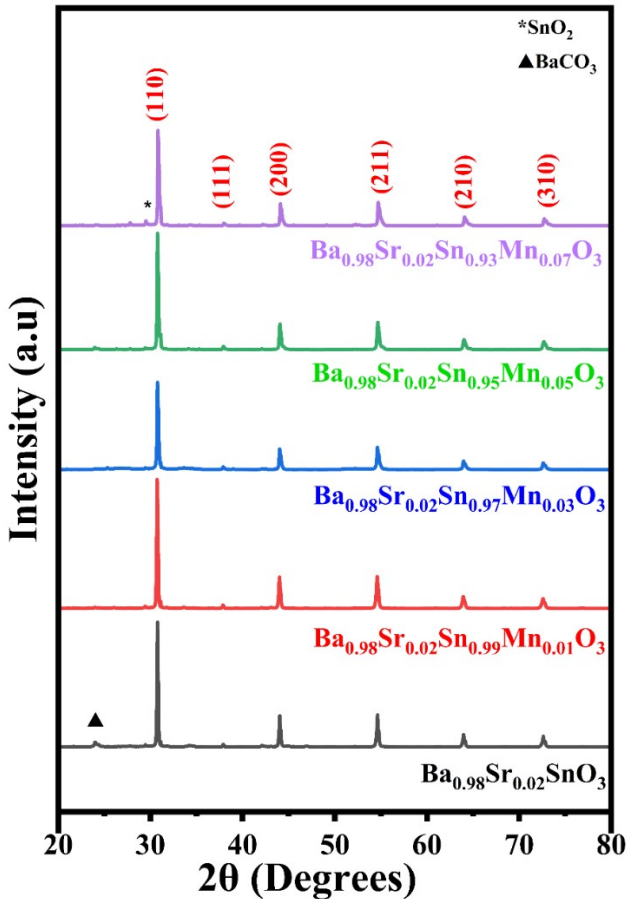

Fig. S1a XRD plots of Mn-doped/undoped $Ba_{0.98}Sr_{0.02}SnO_3$ perovskite.

• Rietveld refinement of $Ba_{0.98}Sr_{0.02}Sn_{0.95}Mn_{0.05}O_3$ perovskite

The Rietveld refinement for sample $Ba_{0.98}Sr_{0.02}Sn_{0.95}Mn_{0.05}O_3$ was carried out using Profex 5.2 version software,[1] having an R_{wp} value of 11.64%, shown in Fig S1b. The refined plot shows the observed, calculated, and difference patterns of $Ba_{0.98}Sr_{0.02}Sn_{0.95}Mn_{0.05}O_3$. The refinement was carried out by taking $BaSnO_3$ as a reference.

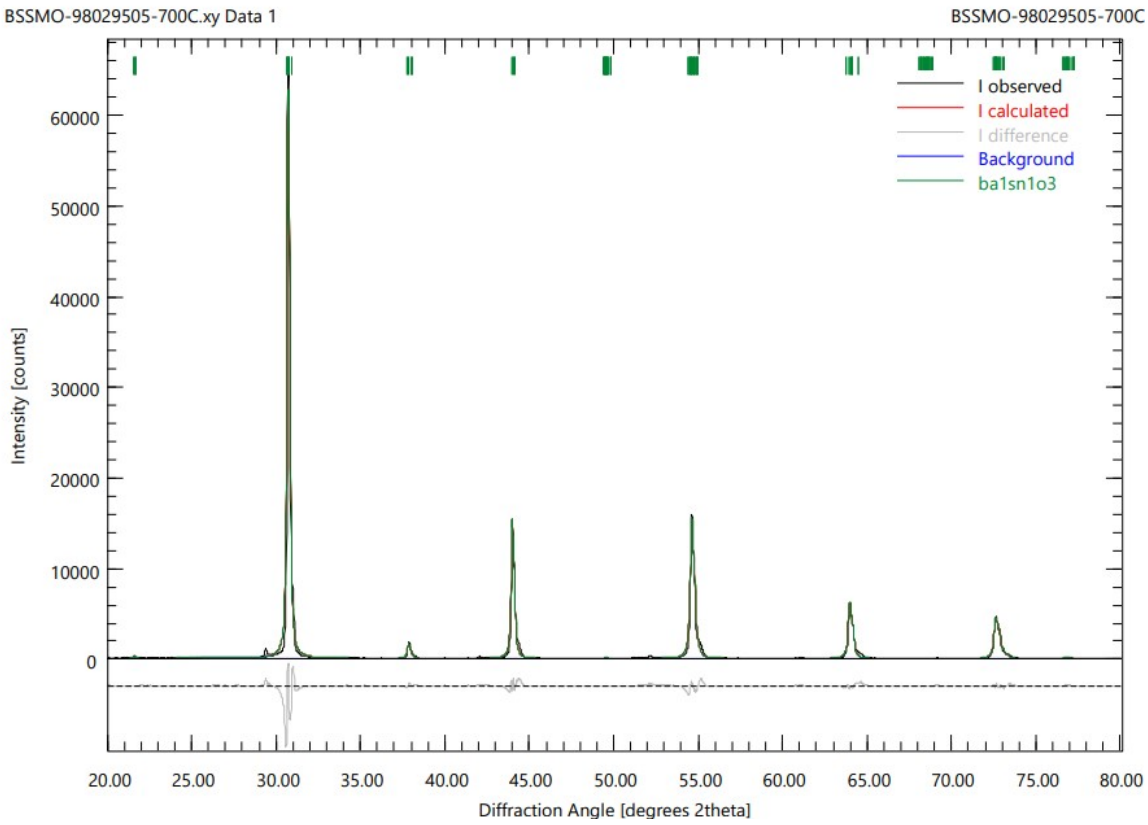

Fig. S1b The plot of the Rietveld refinement, showing the observed, calculated and difference patterns of $Ba_{0.98}Sr_{0.02}Sn_{0.95}Mn_{0.05}O_3$.

• The Williamson-Hall's (W-H) plot of Mn-doped/undoped $Ba_{0.98}Sr_{0.02}SnO_3$ perovskite

The Williamson-Hall's (W-H) plot of all five samples was plotted to determine the crystallite size without strain (Fig S2). The samples' crystallite size was determined using the formula mentioned below.[2]

$$\beta_{Total} \cos \Theta = \varepsilon(4\sin \Theta) + \frac{K\lambda}{D} \qquad \textbf{(1)}$$

It was observed that as the Mn concentration increases, the micro-strain increases.

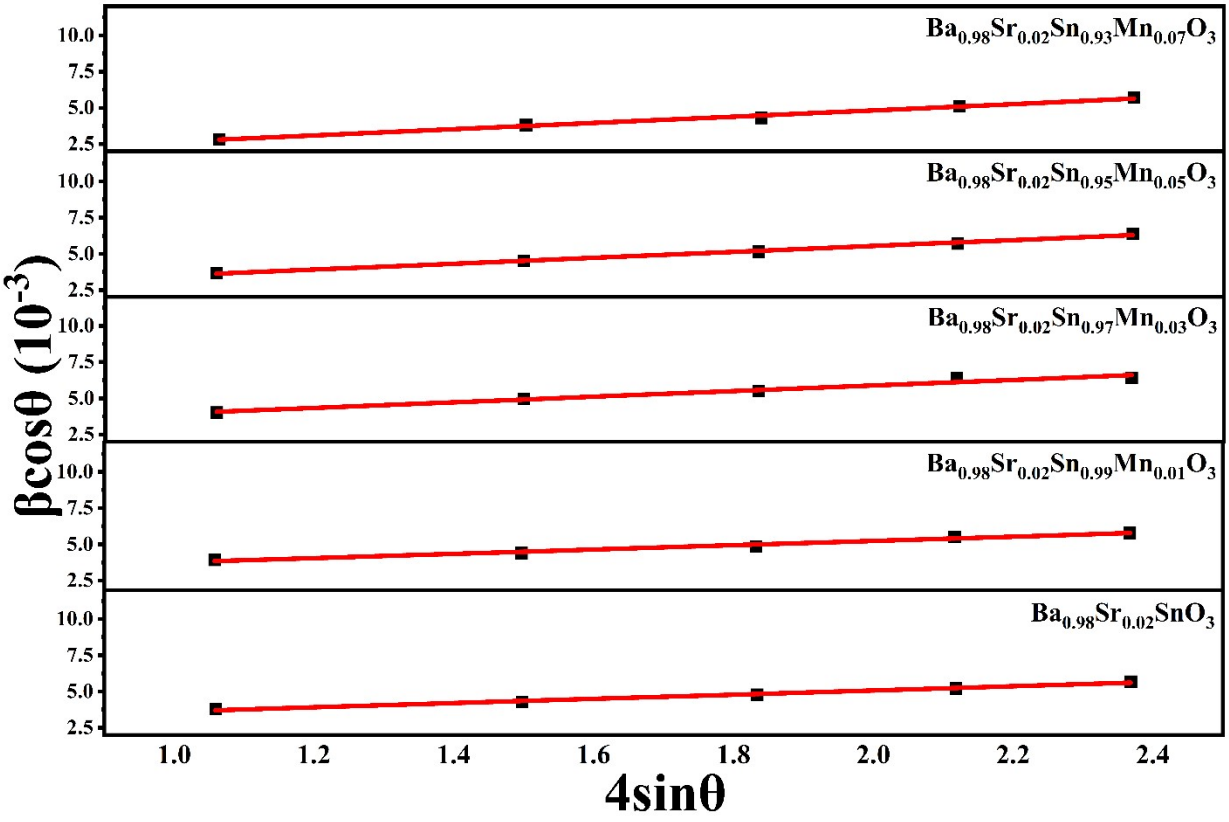

Fig. S2 Williamson-Hall's (W-H) plot with a positive slope for Mn-doped/undoped $Ba_{0.98}Sr_{0.02}SnO_3$ perovskite.

• EDS Analysis of $Ba_{0.98}Sr_{0.02}Sn_{0.95}Mn_{0.05}O_3$ perovskite

The Energy Dispersive X-ray spectroscopy of $Ba_{0.98}Sr_{0.02}Sn_{0.95}Mn_{0.05}O_3$ was carried out to find the atomic and weight percentage of the elements present in the substrate (Fig. S3). The compositional analysis confirms the presence of Ba, Sr, Sn, Mn, and O elements in $Ba_{0.98}Sr_{0.02}Sn_{0.95}Mn_{0.05}O_3$.

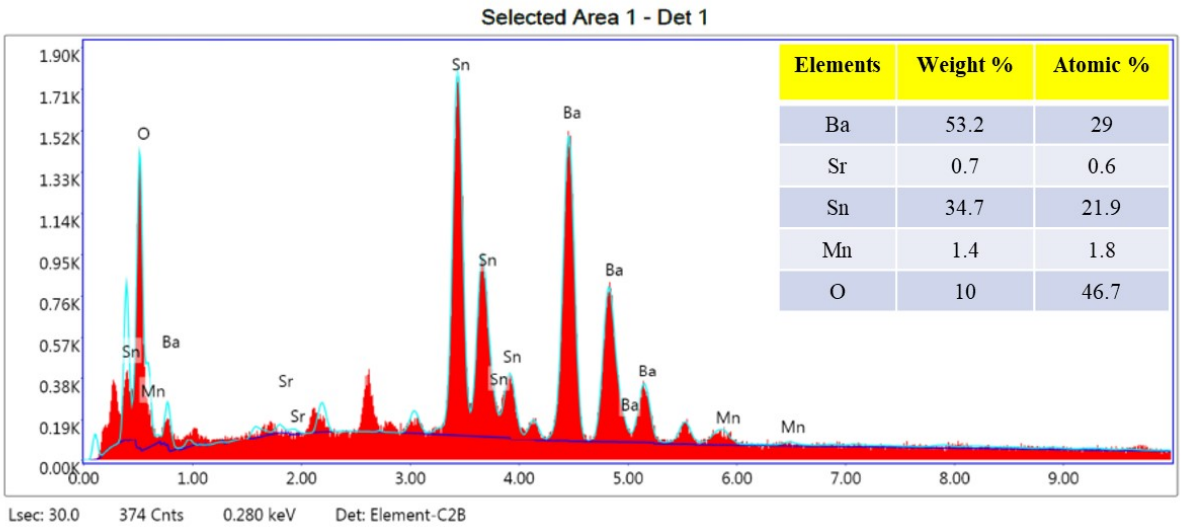

Elements	Weight %	Atomic %
Ba	53.2	29
Sr	0.7	0.6
Sn	34.7	21.9
Mn	1.4	1.8
O	10	46.7

Fig. S3 Energy Dispersive X-ray Spectroscopy plot of $Ba_{0.98}Sr_{0.02}Sn_{0.95}Mn_{0.05}O_3$.

• FESEM images of Mn-doped/undoped $Ba_{0.98}Sr_{0.02}SnO_3$ perovskites

Fig. S4 (a-c), shows the FESEM image of $Ba_{0.98}Sr_{0.02}SnO_3$, $Ba_{0.98}Sr_{0.02}Sn_{0.99}Mn_{0.01}O_3$, and $Ba_{0.98}Sr_{0.02}Sn_{0.97}Mn_{0.03}O_3$ having the cubic morphology along with the rough surface. Fig. S4d shows the FESEM image of $Ba_{0.98}Sr_{0.02}Sn_{0.93}Mn_{0.07}O_3$), which shows the formation of rod-like structures over the cube's surface, which may be of SnO_2. The SnO_2 peaks are visible in the XRD plot of $Ba_{0.98}Sr_{0.02}Sn_{0.93}Mn_{0.07}O_3$.

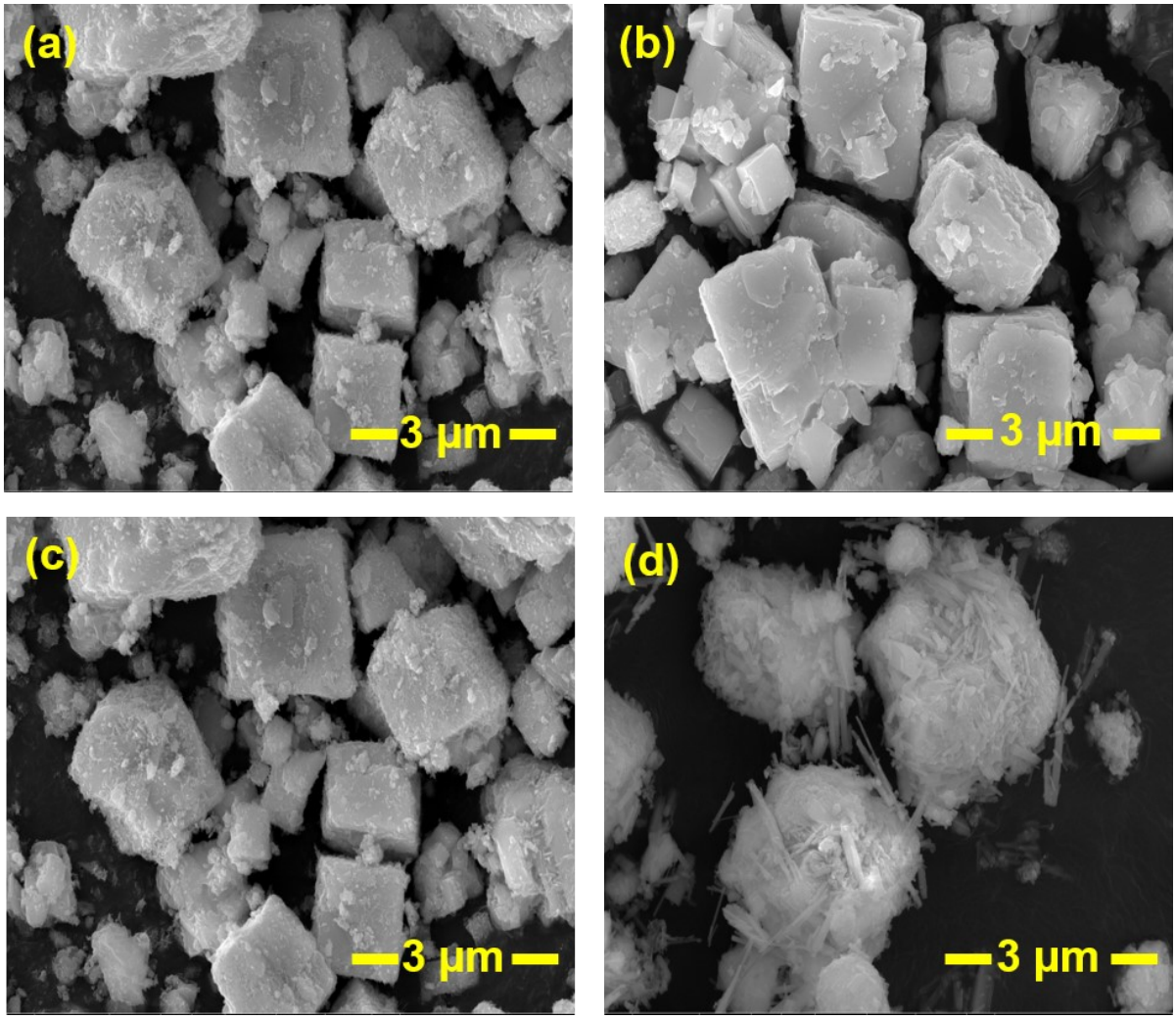

Fig. S4 (a) FESEM image of **(a)** $Ba_{0.98}Sr_{0.02}SnO_3$, **(b)** $Ba_{0.98}Sr_{0.02}Sn_{0.99}Mn_{0.01}O_3$, **(c)** $Ba_{0.98}Sr_{0.02}Sn_{0.97}Mn_{0.03}O_3$, and **(d)** $Ba_{0.98}Sr_{0.02}Sn_{0.93}Mn_{0.07}O_3$, respectively.

• Schematic formation of cubic phase (Ba,Sr)(Sn,Mn)O_3 solid solution via Ostwald Ripening

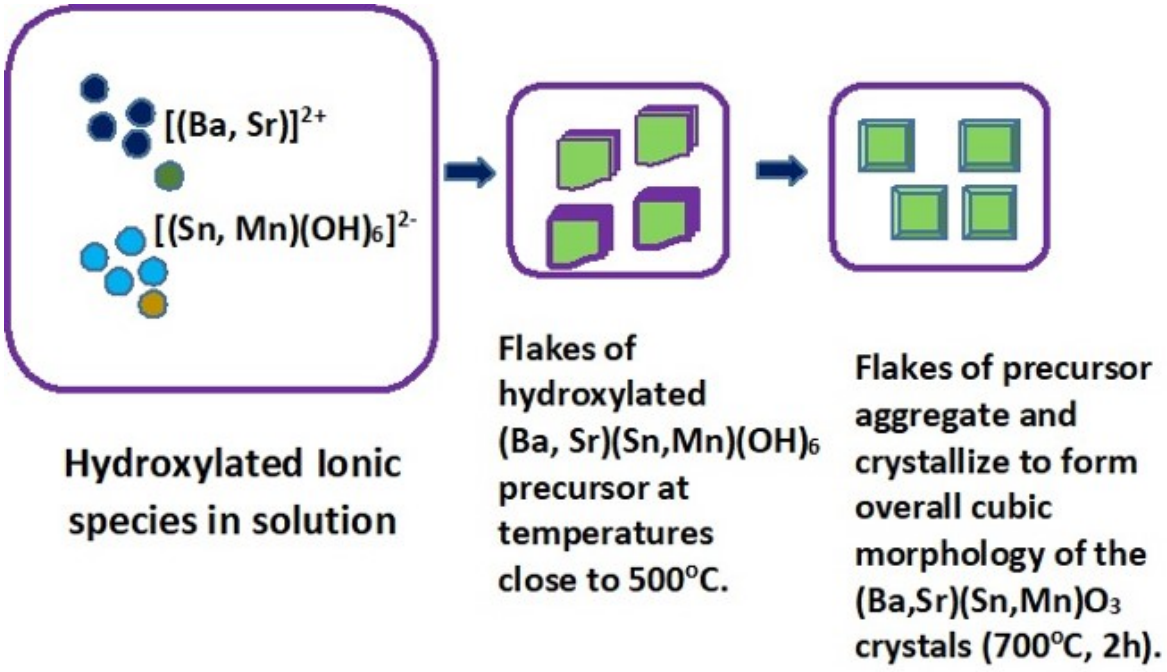

Fig. S5 Formation of cubic morphology for (Ba,Sr)(Sn,Mn)O_3 solid solution via Ostwald Ripening from hydroxylated precursor[3] (For details regarding the solid solution formation, refer to the experimental section of the manuscript).

• Thermogravimetric Analysis

Thermogravimetric-differential scanning calorimetry (TG-DSC) provides very important and vital information relating to the possibility of reaction among the precursors, phase formation and optimization of calcination conditions, and investigation of the thermal stability of the end product. TGA analysis of the sample shows a multistep decomposition reaction and a total 29% mass loss. In Fig. S6, the graph for weight % w.r.t temperature shows the change in weight with an increase in the temperature. 'A' represents the 2.5% wt. loss which is attributed to the loss of physiosorbed surface water and crystalline water and the exothermic peak between 40°C-200°C is attributed to the same. The small kink in the graph, represented as 'B', shows a loss of nitrides and the formation of the intermediate hydroxides [$BaSn(OH)_6$], which is found to be 5%. The DSC curve shows two endothermic peaks at 540 °C and 595 °C showing the loss of nitrides and hydroxides, which is attributed to the formation of

$Ba_{0.98}Sr_{0.02}Sn_{0.95}Mn_{0.05}O_3$ with the major loss of 15%, which is marked as 'C' in Fig. S6, indicating that no crystalline water existed in the compound.[3,4] After 600°C, no weight loss was observed till 800°C in TGA analysis. This indicates that the semiconductor becomes more stable at a calcination temperature of 700°C.

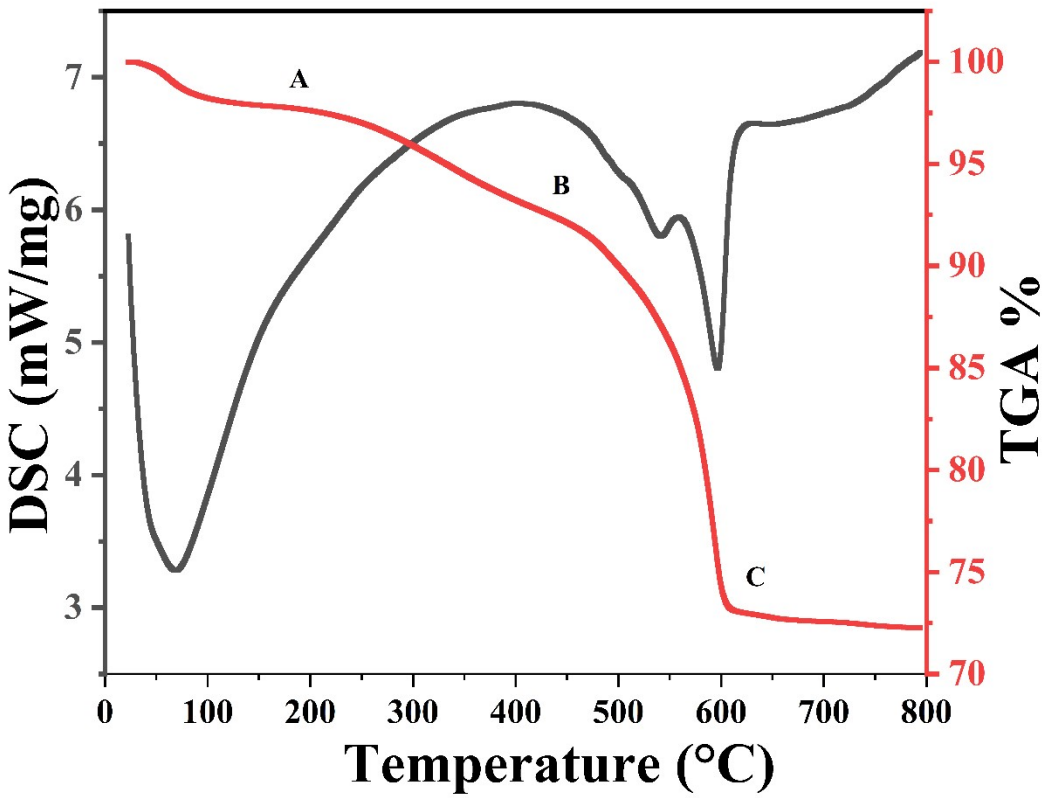

Fig. S6 Thermogravimetric analysis (TGA) (in red) and differential scanning calorimetry (DSC) (in black) curves from 25°C to 800° C of $Ba_{0.98}Sr_{0.02}Sn_{0.95}Mn_{0.05}O_3$.

• Tauc plot of Mn-doped/undoped $Ba_{0.98}Sr_{0.02}SnO_3$ perovskites

Tauc plot shows that the bandgap decreases as the Mn concentration increases. The Tauc's plots plotted to show the indirect bandgap of the Mn-doped/undoped $Ba_{0.98}Sr_{0.02}SnO_3$perovskites semiconductors.[5]

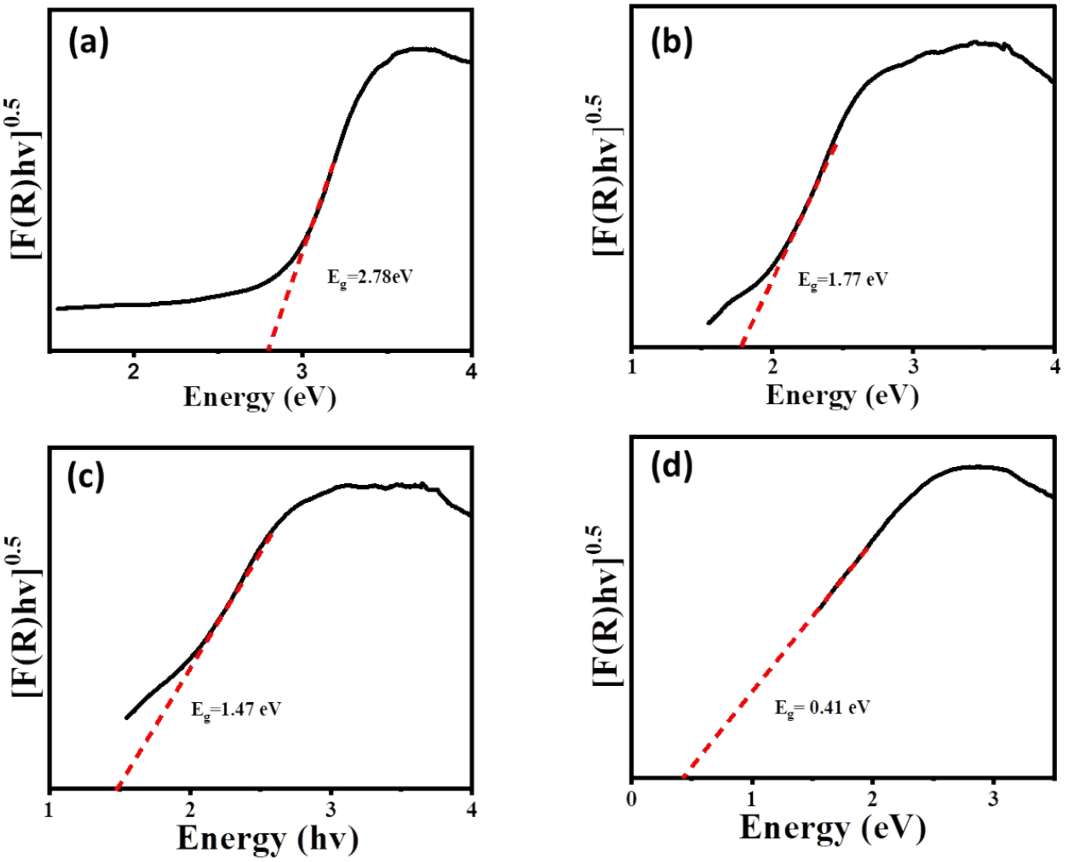

Fig.S7 (a-d) Tauc plots of Indirect bandgap for $Ba_{0.98}Sr_{0.02}SnO_3$, $Ba_{0.98}Sr_{0.02}Sn_{0.99}Mn_{0.01}O_3$, $Ba_{0.98}Sr_{0.02}Sn_{0.97}Mn_{0.03}O_3$, $Ba_{0.98}Sr_{0.02}Sn_{0.95}Mn_{0.05}O_3$, respectively

• Raman analysis of Mn-doped $Ba_{0.98}Sr_{0.02}SnO_3$

The Raman peaks at 143 cm^{-1} and 248 cm^{-1} for $Ba_{0.98}Sr_{0.02}SnO_3$ are attributed to the longitudinal optical and transitional optical phonon modes, respectively.[6,7] Raman analysis shows that, as the Mn concentration increases the peak at 143 cm^{-1} becomes broader and shifts towards the

higher wavelength. The peak at 251 cm^{-1}, flattens with the increase in the concentration of Mn. The 409 cm^{-1} and 450 cm^{-1} peaks merge in the Mn-doped $Ba_{0.98}Sr_{0.02}SnO_3$ due to the distortion in the [SnO_6] octahedra after Mn doping. The peak at 412 cm^{-1} is due to longitudinal optical (LO) phonon vibrations.[8] The peak at 641 cm^{-1} gets broadened with the increase in the concentration of Mn, which is due to the presence of [MnO_6] stretching modes[9,10] and also moves towards a higher wavelength as seen in Fig. S8. The peak at 830 cm^{-1} is attributed to the defect-induced Raman modes.[11] The peak at 1054 cm^{-1} is attributed to the vibrational mode of $BaCO_3$.[12]

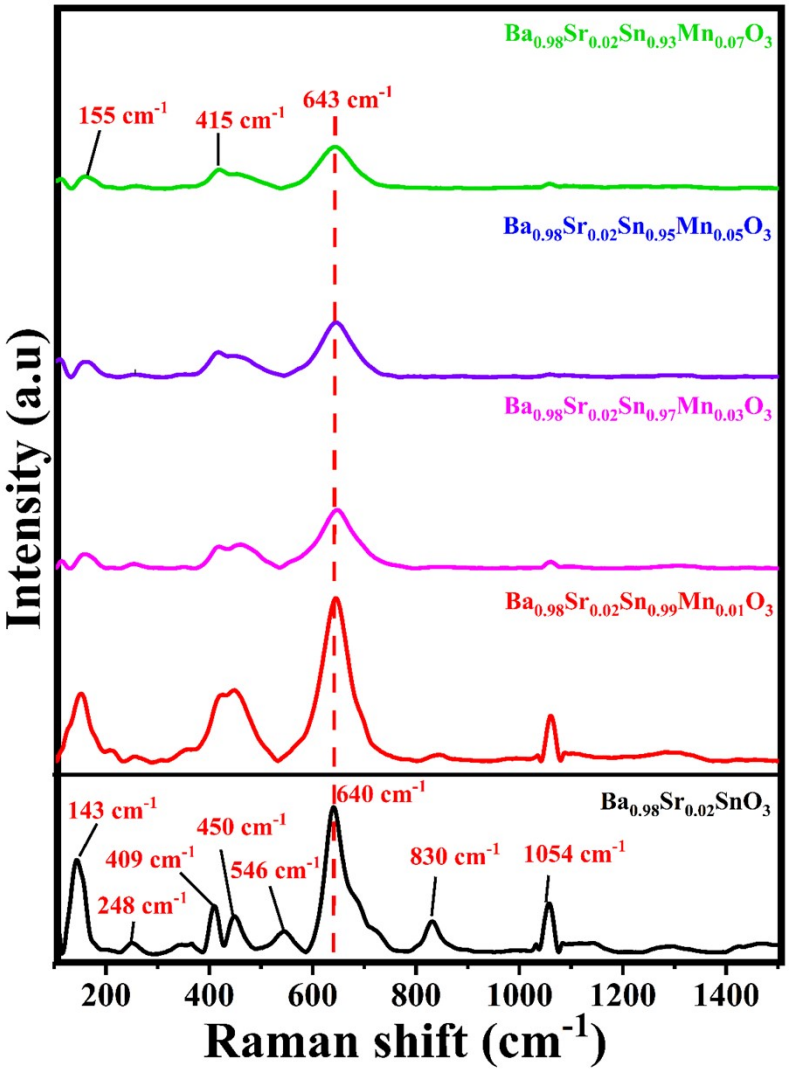

Fig S8. Raman spectra of Mn-doped and undoped $Ba_{0.98}Sr_{0.02}SnO_3$ perovskites

• **Experimental Setup for Sensor Analysis**

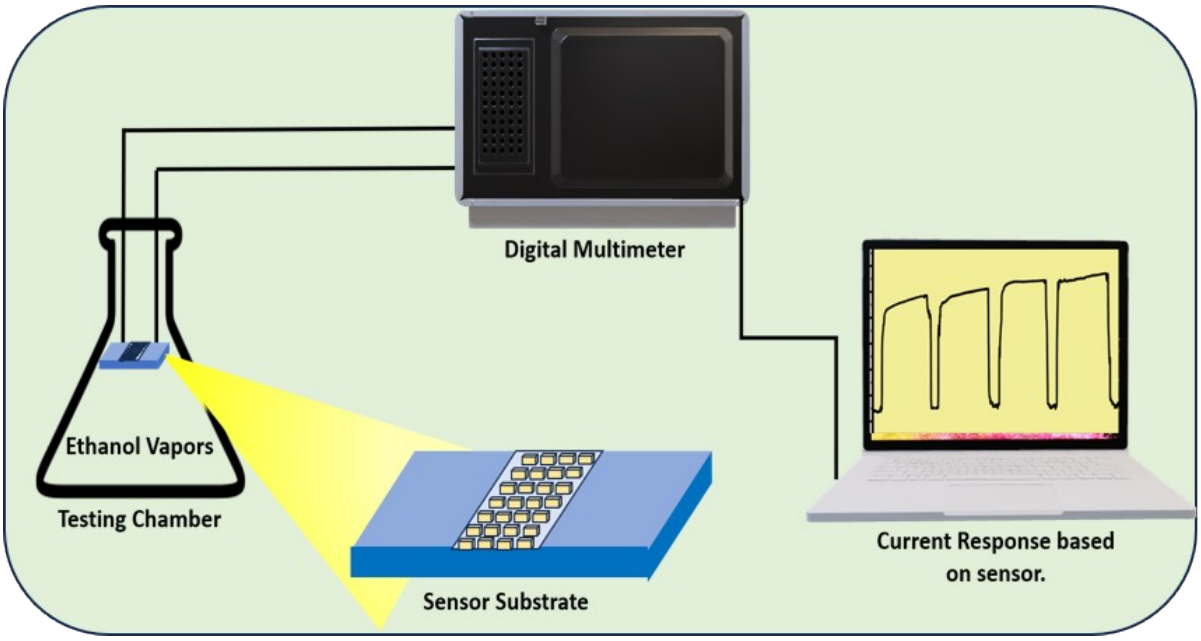

Fig S9a. The Schematic representation of the experimental setup for sensing VOCs.

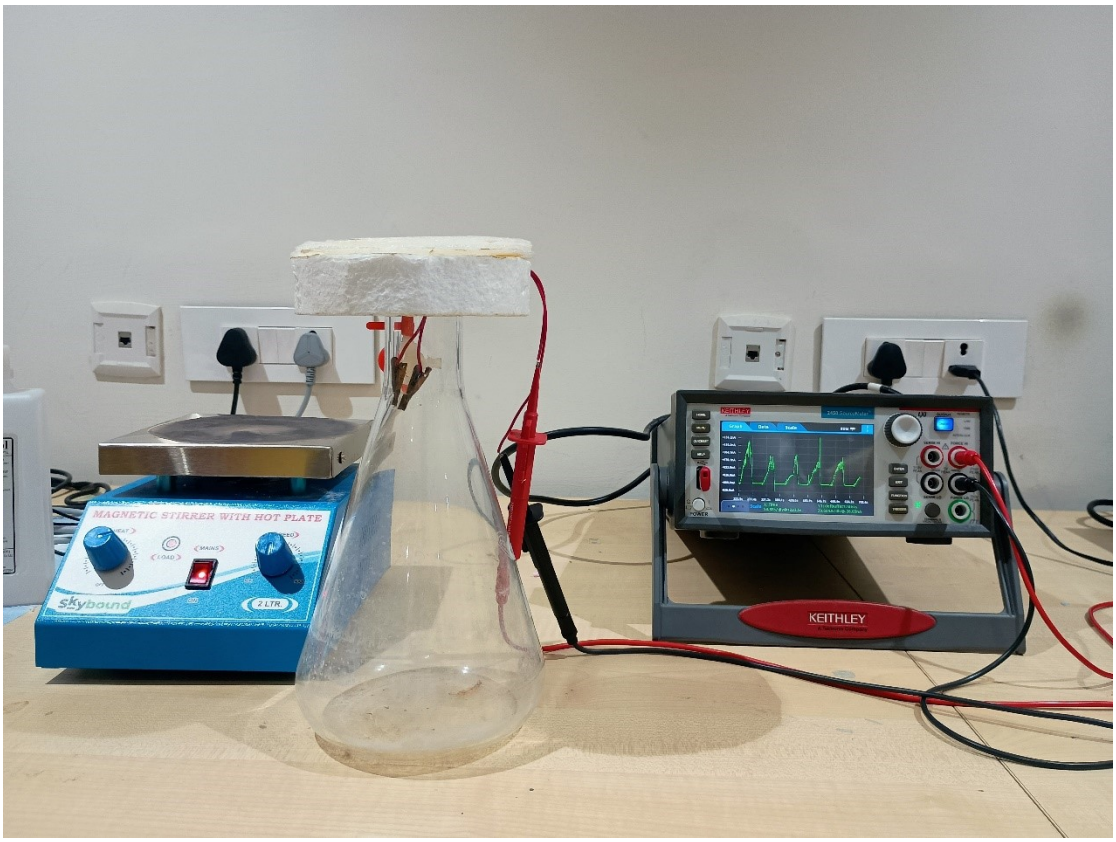

Fig S9b. The actual experimental setup for sensing VOCs in the lab.

• Sensor Response of $Ba_{0.98}Sr_{0.02}Sn_{0.95}Mn_{0.05}O_3$ perovskite for 100 ppm EtOH at r.t and 85% humidity

The Sensor response vs Time plot for $Ba_{0.98}Sr_{0.02}Sn_{0.95}Mn_{0.05}O_3$ after 5 months at a humidity of 85%. The time scale on the x-axis depends on the devices under consideration. The time scale may range from a few seconds,[13-15] minutes, and hours and also on the pulse scale.

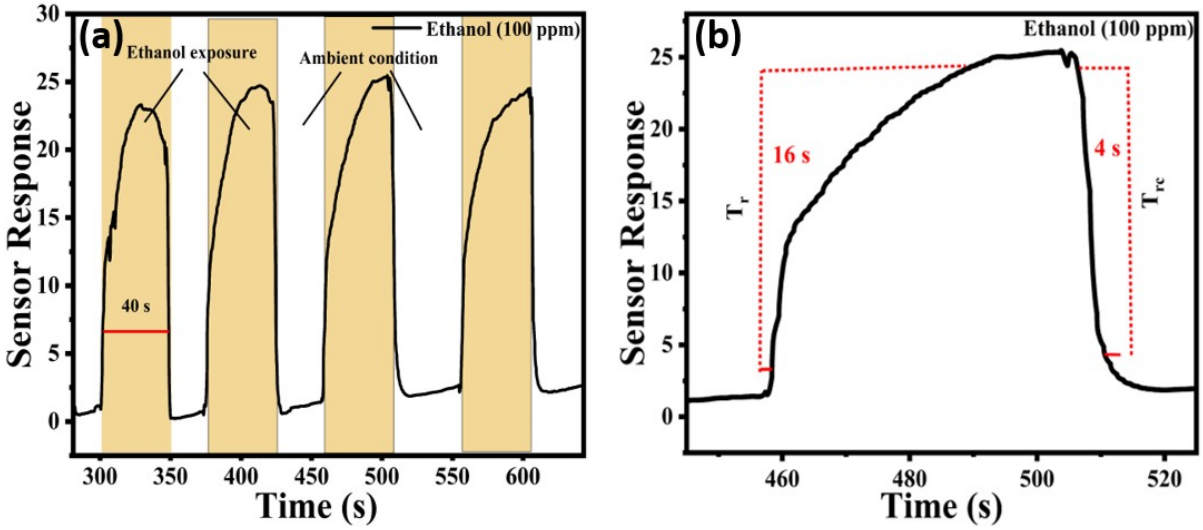

Fig. S10 (a) The Sensor response vs Time plot and **(b)** Response and recovery time of $Ba_{0.98}Sr_{0.02}Sn_{0.95}Mn_{0.05}O_3$ perovskite recorded after 5 months at a humidity of 85%

• **Computational studies**

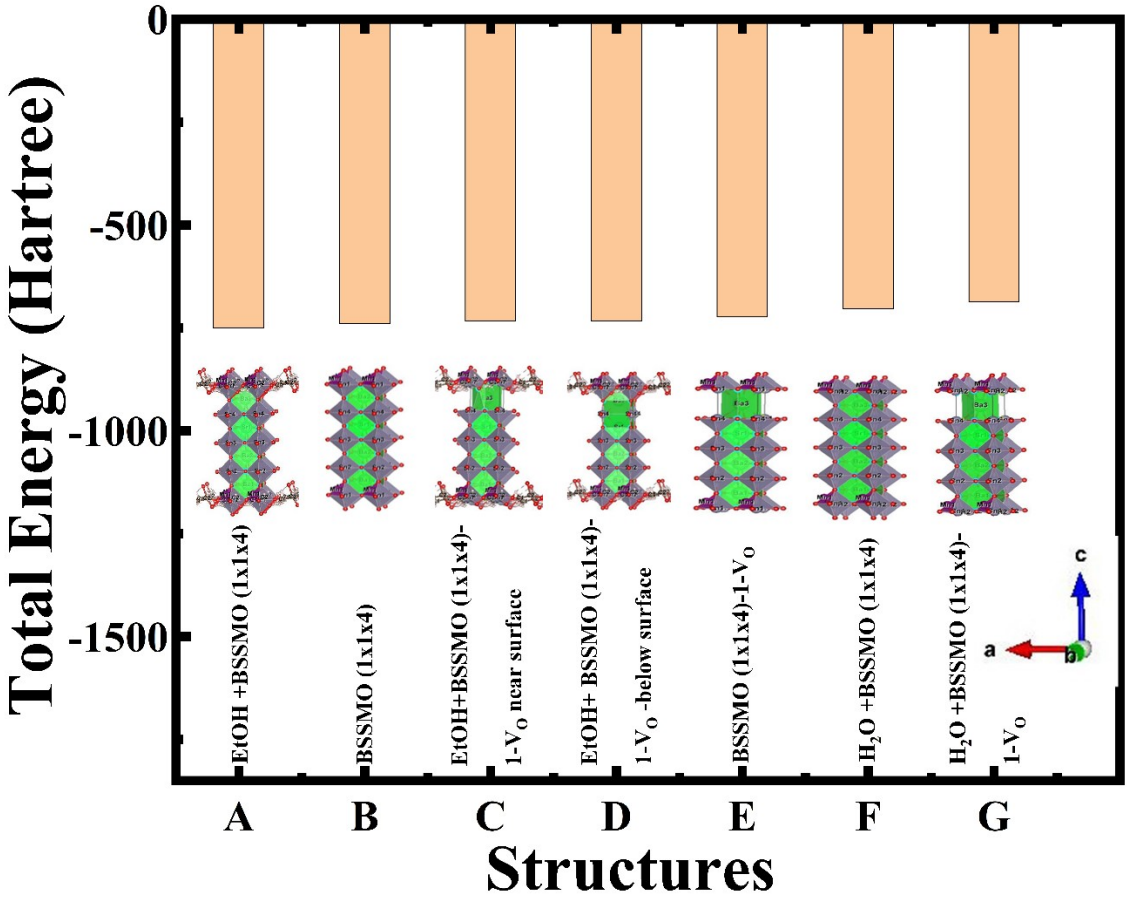

Fig. S11a Comparison of DFT-based converged Total Energy values of structurally optimized 1 x 1 x 4 (Ba,Sr)(Sn, Mn)O_3 in the presence and absence of polar molecules (Ethanol and Water) in the ground state.

[**Note:** Here BSSMO in the above is the abbreviation used for (Ba,Sr)(Sn, Mn)O_3.]

Computational Method used: The supercell (1 x 1 x 4) (abbreviated as BSSMO) and the corresponding coordinate file (number of atoms in supercell range from 20 to 30) are built using the Avogadro builder platform[16] using a $BaSnO_3$ .cif file (Details of BSSMO: Sr/Ba = 0.25, Mn and O-vacancies (V_o) are introduced at arbitrary sites close to the surface, Insert 1 polar molecule Ethanol or water close to surface and compute). The self-consistent field (SCF) density functional theory (DFT) computation in the ground state has been carried out on the built supercell using plane wave pseudopotentials (version PSP8: ONCVPSP-3.2.3.1) for all the atoms using GGA-PBE exchange-correlation at an energy cut-off value of 25 Hartrees

(~680 eV) at 2 x 2 x 1 r-centered k-point grid, as implemented in ABINIT (Version 8.8.1) Program.[17] The SCF convergence of these supercells has been achieved in the presence of polar molecules. All supercell-based computations converged (convergence criteria: ΔE smaller than 10^{-10} Ha between successive iterations) in less than 30 steps, indicating a favourable orientation of polar molecule C_2H_5OH in the structure along the edges of the Sn/Mn polyhedra as per visualization using VESTA.[18] These favourable orientations would facilitate ethanol oxidation. Two enlarged supercell structures, A and C, are shown below to delineate these structural attributes. Computed minimum energy atomic coordinate of Mn = (0.219, 0.219, 0.055)

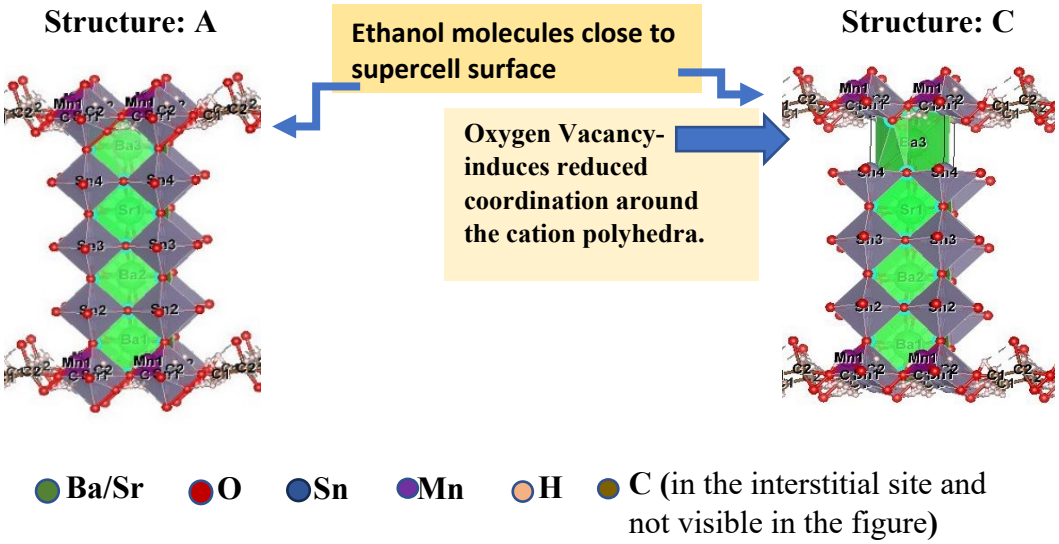

Fig. S11b DFT optimised supercell models in the ground state; **Structure A (projected in the same orientation as in Fig. S11a):** EtOH +(Ba,Sr)(Sn,Mn)O_3 (1x1x4) supercell (30 atoms in the supercell)
Structure C (projected in the same orientation as in Fig. S11a): EtOH +(Ba,Sr)(Sn,Mn)O_3 (1x1x4) supercell + O-vacancy (29 atoms is the supercell).

[A sample input file for SCF-DFT for Structure A in the ground state is given below:
 # BSSO-114-Et-input-ABC
 # abinit input generated by Avogadro plugin
 # abinit found at
 # basis set, bands, k-points, SCF tolerance
ecut 25
occopt 1
tsmear 0.01

```
ngkpt 2 2 1
nshiftk 1
shiftk
 0 0 0
toldfe 1e-10
# super cell
acell 4.11 4.11 16.44 Angstr
angdeg 90 90 90
chkprim 0
# Atomic positions and species
natom 30
xangst
      2.05500       2.05500       2.05500
      0.00000       0.00000       0.00000
      0.00000       2.05500       0.00000
      0.00000       0.00000       2.05500
      2.05500       0.00000       0.00000
      2.05500       2.05500       6.16500
      0.00000       0.00000       4.11000
      0.00000       2.05500       4.11000
      0.00000       0.00000       6.16500
      2.05500       0.00000       4.11000
      2.05500       2.05500      10.27500
      0.00000       0.00000       8.22000
      0.00000       2.05500       8.22000
      0.00000       0.00000      10.27500
      2.05500       0.00000       8.22000
      2.05500       2.05500      14.38500
      0.00000       0.00000      12.33000
      0.00000       2.05500      12.33000
      0.00000       0.00000      14.38500
      2.05500       0.00000      12.33000
      1.62654      -0.03769       0.84561
      1.01120      -0.04529      -0.06260
      1.32526       0.80309      -0.68470
      1.25012      -0.96118      -0.61889
     -0.46208       0.03063       0.29470
     -0.75800      -0.82632       0.93156
     -0.68222       0.95369       0.86656
     -1.19813       0.01809      -0.90724
     -2.11270       0.06498      -0.66499
      0.90000       0.90000       0.90000
ntypat 7
znucl 1  6  8  25  38  50  56
typat 7  6  3  3  3  7  6  3  3  3  5  6  3  3  3  7  6  3  3  3  1  2  1  1  2  1  1  3  1  4


# Geometrical relaxation
ionmov 0
ntime 10
tolmxf 0.00005
dilatmx 1.05000
ecutsm 0.50000]
```

Table S1. The concentration of EtOH, sensing temperature, response, and recovery time of ethanol gas sensor prepared using different metal oxide/noble metal, metal oxide/metal oxide, metal oxide/metal sulphide, and metal oxide/other materials heterojunction structures.

Ref.	Composites	Conc^{n}. of EtOH (ppm)	Temp (°C)	Response Time (s)	Recovery Time (s)
19	Ag/In_2O_3	50	220	8	13
20	Ag/ZnO	200	300	2	3
21	Au/SnO_2	100	240	4	48
22	α-Fe_2O_3/ZnO/Au	100	80	4	5
23	NiO/SnO_2	100	rt	23	13
24	SnO_2/TiO_2	100	240	8	10
25	CuO/ZnO	100	240	6	18
26	ZnO/g-C_3N_4	500	350	25	45
27	In_2O_3/ZnS	100	260	21	34
28	$Fe/TiO_2/MoS_2$	5	rt	43	47
29	α-Fe_2O_3/MoS_2	100	rt	6	5
30	r-GO/Co_3O_4	100	180	24	4
31	ZnO/R-GO/g-C_3N_4	100	300	76	6
32	Sb/SnO_2	50	rt	259	214
33	$BaSnO_3$	100	260	15.5	13
This Work	**$Ba_{0.98}Sr_{0.02}Sn_{0.95}Mn_{0.05}O_3$** (At Humidity ~55%)	**100**	**rt**	**1.06**	**1.81**

References

1. N. Doebelin and R. Kleeberg, *J. Appl. Crystallogr.*, 2015, **48**, 1573–1580.
2. K. H. Moon, Y.-I. Kim and C.-S. Park, *Ceram. Int.*, 2016, **42**, 1432–1438.
3. H. Mizoguchi, N. S. P. Bhuvanesh, Y. Il Kim, S. Ohara and P. M. Woodward, *Inorg. Chem.*, 2014, **53**, 10570–10577.
4. T. Roy, S. Sahani, D. Madhu and Y. Chandra Sharma, *J Clean Prod*, 2020, **265**, 121440.
5. N. Rajamanickam, K. Jayakumar and K. Ramachandran, *J. Mater. Sci: Mater Electron,* 2018, **29**, 19880–19888.
6. T. N. Stanislavchuk, A. A. Sirenko, A. P. Litvinchuk, X. Luo and S. W. Cheong, *J. Appl. Phys.*, 2012,**112**, 0–7.

7. M. Avinash, M. Muralidharan and K. Sivaji, *Physica. B Condens. Matter,* 2019, **570**, 157–165.
8. K. Balamurugan, N. Harish Kumar, B. Ramachandran, M. S. Ramachandra Rao, J. Arout Chelvane and P. N. Santhosh, *Solid State Commun.*, 2009, **149**, 884–887.
9. J. John, M. Dhananjaya, S. Suresh, S. Savitha Pillai, M. Sahoo, O. M. Hussain, R. Philip and V. P. Mahadevan Pillai, *J Mater Sci: Mater. Electron*, 2020, **31**, 11159–11176.
10. K. K. James, P. S. Krishnaprasad, K. Hasna and M. K. Jayaraj, *J. Phys. Chem. Solids*, 2015, **76**, 64–69.
11. J. Cerdà, J. Arbiol, R. Diaz, G. Dezanneau and J. R. Morante*, Mater. Lett.,* 2002, **56**, 131–136.
12. P. Makuła, M. Pacia and W. Macyk, *J Phys Chem Lett*, 2018, **9**, 6814–6817.
13. J. Dai, G. Xie, C. Chen, Y. Liu, H. Tai, Y. Jiang and Y. Su, *Appl Phys Lett.*, 2024, **124**, 053701.
14. C. Chen, G. Xie, J. Dai, W. Li, Y. Cai, J. Li, Q. Zhang, H. Tai, Y. Jiang and Y. Su, *Nano Energy*, 2023, **116**,108788.
15. J. Huang, Y. Cai, G. Xie, X. Xu, Z. Geng, Y. Jiang and Y. Su, *Wearable Electronics*, 2024, **1**, 180–188.
16. M. D. Hanwell, D. E. Curtis, D. C. Lonie, T. Vandermeersch, E. Zurek, G. R. Hutchison, *J. Cheminformatics, 2012,* **4**, 17.
17. X. Gonze et al, *Comp. Phys. Commun.*, 2016, **205,** 106-131.
18. K. Momma, F. Izumi, *J. Appl. Crystallogr,* 2011,**44**, 1272-1276.
19. X. Liu, X. Sun, X. Duan, C. Zhang, K. Zhao and X. Xu, *Sens. Actuators B Chem*, 2020, **305**, 127450.
20. H. Wang, Q. Li, X. Zheng, C. Wang, J. Ma, B. Yan, Z. Du, M. Li, W. Wang and H. Fan, *J Alloys Compd*, *J. Alloys Compd.*, 2020, **829**, 154453.
21. Y. Liu, X. Li, Y. Wang, X. Li, P. Cheng, Y. Zhao, F. Dang and Y. Zhang, *Sens. Actuators B Chem.*, 2020, **319**, 128299.
22. Y. Chen, H. Li, Q. Ma, Q. Che, J. Wang, G. Wang and P. Yang, *Appl. Surf. Sci.*, 2018, **439**, 649–659.
23. N. Jayababu, M. Poloju, J. Shruthi and M. V. R. Reddy, *Ceram. Int.*, 2019, **45**, 15134–15142.
24. K. Chen, S. Chen, M. Pi and D. Zhang, *Solid State Electron*, 2019, **157**, 42–47.
25. M. Yin, F. Wang, H. Fan, L. Xu and S. Liu, *J. Alloys Compd.*, 2016, **672**, 374–379.
26. J. Cao, Y. Gong, Y. Wang, B. Zhang, H. Zhang, G. Sun, H. Bala and Z. Zhang, *Mater. Lett.*, 2017, **198**, 76–80.
27. Q. Chen, S. Y. Ma, X. L. Xu, H. Y. Jiao, G. H. Zhang, L. W. Liu, P. Y. Wang, D. J. Gengzang and H. H. Yao, *Sens. Actuators B Chem.*, 2018, **264**, 263–278.
28. J. Wu, D. Zhang and Y. Cao, *J. Colloid Interface Sci.*, 2018, **529**, 556–567.
29. D. Zhang, X. Fan, A. Yang and X. Zong, *J. Colloid Interface Sci.*, 2018, **523**, 217–225.
30. D. Wang, Y. Yu, H. He, J. Wang, W. Zhou and H. D. Abruña, *ACS Nano*, 2015, **9**, 1775–1781.
31. F. Meng, Y. Chang, W. Qin, Z. Yuan, J. Zhao, J. Zhang, E. Han, S. Wang, M. Yang, Y. Shen and M. Ibrahim, *ACS Appl. Nano Mater.*, 2019, **2**, 2734–2742.

32. R. Ramanathan, S. Nagarajan, S. Sathiyamoorthy, B. Manavaimaran, H. C. Barshilia and R. C. Mallik, *Mater. Adv.*, 2023, **5**, 293–305.
33. A. Bhattacharya, X. Chu, Y. Dong, S. Liang and A. K. Chakraborty, *Vacuum*. 2020, **180**, 109645.

==========